Journal of Power Sources 203 (2012) 84–96

Contents lists available at SciVerse ScienceDirect

Journal of Power Sources

journal homepage: www.elsevier.com/locate/jpowsour

Thermal–electrochemical model for passive thermal management of a spiral-wound lithium-ion battery

Karthik Somasundaram[a], Erik Birgersson[b,*], Arun Sadashiv Mujumdar[a]

[a] Department of Mechanical Engineering, National University of Singapore, Singapore 117576, Singapore
[b] Department of Chemical and Biomolecular Engineering, National University of Singapore, Singapore 117576, Singapore

ARTICLE INFO

Article history:
Received 18 October 2011
Received in revised form
22 November 2011
Accepted 24 November 2011
Available online 6 December 2011

Keywords:
Li-ion battery
Modeling
Passive cooling
Phase change material
Spiral-wound
Thermal management

ABSTRACT

Safe and reliable operation of a Li-ion battery requires control and often management of the thermal envelope. In this context, a two-dimensional, transient mathematical model comprising conservation of charges, species, and energy together with electroneutrality, constitutive relations and relevant initial and boundary conditions for a spiral-wound cylindrical Li-ion battery is derived and solved numerically for passive thermal management with and without a phase change material (PCM) at various galvanostatic discharge rates. Two-way coupling of the electrochemical and thermal equations of change is attained through heat generation terms and temperature-dependent physical properties. Within this framework, the electrochemical and thermal behavior is discussed in terms of edge effects arising from the design of the spiral-wound structure and variations in heat generation in the functional layers. In addition, the cell performance with passive thermal management through a PCM is shown to lower the overall temperature of the cell at discharge rates around 5 C-rates, provided the PCM layer is thick enough to provide cooling during the entire discharge. The model can be employed for wide-ranging parameter studies as well as multi-objective optimization of not only design parameters pertaining to the spirals but also, for example, for design of the thickness of the PCM layer.

1. Introduction

Recent years have seen several recalls of commercial Li-ion batteries due to overheating. The heat originates mainly from the electrochemical reactions that occur during charge/discharge of the battery as well as Joule heating – if this heat is not dissipated properly, it can lead to overheating of the battery, and, in a worst-case scenario, thermal runaway. The latter typically occurs in conjunction with 'abuse' conditions, high power draw, and/or manufacturing defects. Generally, some form of protection is thus needed to prevent overheating, either by means of electronic control circuits that monitor charge/discharge rates and/or temperature, or by means of a properly designed thermal management system. Furthermore, for the purpose of operating the battery within safe operating temperature limits, either one of two following thermal management strategies are typically introduced: active systems with air/liquid cooling [1] or passive systems with, for example, phase-change materials (PCMs) [1–6]; see Bandhauer et al. [7] for a detailed review of these. The main advantages of passive cooling with PCM viz-a-viz active cooling are a simplified design, absence of parasitic power consumption, smaller temperature gradients with air as coolant under normal and stressed operating conditions [1], and that propagation of energy from cell to cell arising from thermal runaway inside a battery pack can be reduced [5].

Various mechanistic mathematical models have been developed in order to predict the transient electrochemical and thermal behavior of a Li-ion cell in a rectilinear geometry [8–17] and a spiral-wound geometry [18–25]. In essence, these models typically consider the transient equations of change for species, charge and energy together with relevant boundary conditions and constitutive relations. The level of detail and resolution depends on the treatment of electrochemical and thermal phenomena: the most detailed models [11,13–15] solve the governing equation in the form of partial differential equations (PDEs), thus resolving the *local* transport phenomena, electrochemistry and heat generation. Loss of detail is often incurred when one of the governing equations is simplified to an ordinary differential equation (ODE) or a phenomenological expression, thus only truly accounting for the *global* behavior of the battery cell and, to a lesser extent, the local behavior; for example, when only the equation of change for energy is solved locally together with an expression for heat generation from some form of approximative relation [17–19,21,22,24] of the electrochemical reactions or from experimental measurements [1,5]; or when the equations of change describing the electrochemical phenomena on a local level are coupled with some form of

* Corresponding author. Tel.: +65 6516 7132; fax: +65 6779 1936.
E-mail address: chebke@nus.edu.sg (E. Birgersson).

0378-7753/$ – see front matter © 2011 Elsevier B.V. All rights reserved.
doi:10.1016/j.jpowsour.2011.11.075

Nomenclature

a_i	constants in electrolyte conductivity expression
$\mathcal{A}$	specific interfacial area per unit volume (m^{-1})
C_i	electrode capacity ($Ah\,m^{-2}$)
C_{th}	theoretical capacity of electrode material ($mAh\,g^{-1}$)
c_l	electrolyte concentration ($mol\,m^{-3}$)
c_l^0	initial electrolyte concentration ($mol\,m^{-3}$)
C_p	effective specific heat capacity ($J\,(kg\,K)^{-1}$)
c_s^0	initial concentration of lithium in the active material ($mol\,m^{-3}$)
c_s	concentration of lithium in the active material ($mol\,m^{-3}$)
c_s^{avg}	average concentration of lithium in the active material ($mol\,m^{-3}$)
c_s^{max}	maximum concentration of lithium in the active material ($mol\,m^{-3}$)
c_s^{surf}	surface concentration of lithium in the active material in the electrodes ($mol\,m^{-3}$)
D_l	diffusion coefficient of electrolyte ($m^2\,s^{-1}$)
D_s	diffusion coefficient of lithium in the active material ($m^2\,s^{-1}$)
$E_{a,\Theta}$	activation energy for a variable Θ ($kJ\,mol^{-1}$)
F	Faraday's constant (96,487 $C\,mol^{-1}$)
h	height of the battery (m)
$\mathfrak{h}$	heat transfer coefficient ($W\,m^{-2}\,K^{-1}$)
i_{app}	applied current density ($A\,m^{-2}$)
i_0	exchange current density ($A\,m^{-2}$)
$\mathbf{i}_l$	liquid phase current density ($A\,m^{-2}$)
$\mathbf{i}_s$	solid phase current density ($A\,m^{-2}$)
i_f	faradaic transfer current density ($A\,m^{-2}$)
J	local charge transfer current per unit volume ($A\,m^{-3}$)
k	effective thermal conductivity ($W\,(m\,K)^{-1}$)
k_0	reaction rate constant
L	latent heat of PCM ($J\,kg^{-1}$)
$\mathcal{L}$	length of the spiral (m)
l_s	diffusion length (m)
w_i	thickness of the layer i (m)
$\mathbf{N}_l$	species (lithium ion) flux ($mol\,m^{-2}\,s^{-1}$)
$\mathbf{n}$	normal vector
$\mathfrak{ni}$, $\mathfrak{pi}$	constants in the entropic heat term for negative and positive electrodes
$i\mathfrak{N}$, $i\mathfrak{P}$	constants in the open circuit potential for negative and positive electrodes
Q	volumetric heat generation ($W\,m^{-3}$)
$\mathbf{q}$	conductive heat flux ($W\,m^{-2}$)
R	gas constant $J\,(mol\,K)^{-1}$
R_b	radius of battery (type 18650) (m)
$\mathfrak{R}$	radius of active material in the electrodes (m)
t	time (s)
t_+^0	transference number of cation
T	temperature (K)
T_s	start temperature of phase change (K)
T_l	end temperature of phase change (K)
$U_{ref,i}$	open circuit potential of the electrode i (V)
$\mathfrak{x}$	number of moles of Li in C_6
$\mathfrak{y}$	number of moles of Li in Mn_2O_4

Greek letters

α_a	anodic transfer coefficient
α_c	cathodic transfer coefficient
ε_l	volume fraction of electrolyte
ε_f	volume fraction of conductive filler additive
ε_p	volume fraction of polymer phase
η	overpotential
θ_{ne}	state of charge of negative electrode
θ_{pe}	state of charge of positive electrode
ν_+, ν_-	number of cations and anions into which a mole of electrolyte dissociates
ξ	emissivity of the outer can material
ρ	effective density ($kg\,m^{-3}$)
σ	Stefan–Boltzmann constant ($W\,m^{-2}\,K^{-4}$)
σ_l	ionic conductivity of electrolyte ($S\,m^{-1}$)
σ_s	electronic conductivity of solid matrix ($S\,m^{-1}$)
ϕ_l	liquid phase potential (V)
ϕ_s	solid phase potential (V)
ϕ_l^0	initial liquid phase potential (V)
ϕ_s^0	initial solid phase potential (V)
$\Theta(T)$	placeholder for a temperature dependent property

Subscripts

amb	ambient
cc	current collector
el	electrolyte
ne	negative electrode
pe	positive electrode
ref	reference value
sp	separator

Superscripts

0	initial value
eff	effective value

lumped-parameter model for the thermal part on the global level [25,26]. The general trend here is that detailed local models have been employed for rectilinear geometries and simplified counterparts for spiral-wound geometries – the latter is typically significantly more expensive to solve from the numerical point-of-view as can be inferred from intricate geometrical features in Fig. 1.

In view of the lack of detailed, local resolution for modeling and simulation of coupled electrochemistry, transport phenomena and heat generation in spiral-wound geometries, the aim of this work is twofold: First, to develop a coupled thermal–electrochemical model for a cylindrical spiral-wound lithium-ion battery without compromising local resolution, which can easily be applied to spiral-wound prismatic cells as well; and second, to apply the derived model to investigate the design and operation of a passive thermal management system based on PCM. In short, the model considers transient conservation of charges, species and energy; it couples the electrochemical and thermal behavior through the heat generation arising from reversible, irreversible and ohmic heating as well as through the temperature-dependent transport and electrochemical parameters. The PCM, in turn, is wrapped around the battery and solved for in terms of conservation of energy. The results are discussed with emphasis on transient behavior and temperature distribution in the various layers of the spiral-wound battery under galvanostatic discharge at various rates.

2. Mathematical formulation

We consider a commercially available spiral-wound cylindrical Li-ion 18650 battery (Fig. 1a), for which we resolve a two-dimensional cross-section of the battery, as illustrated in Fig. 1b, where the functional layers – positive electrode (pe),

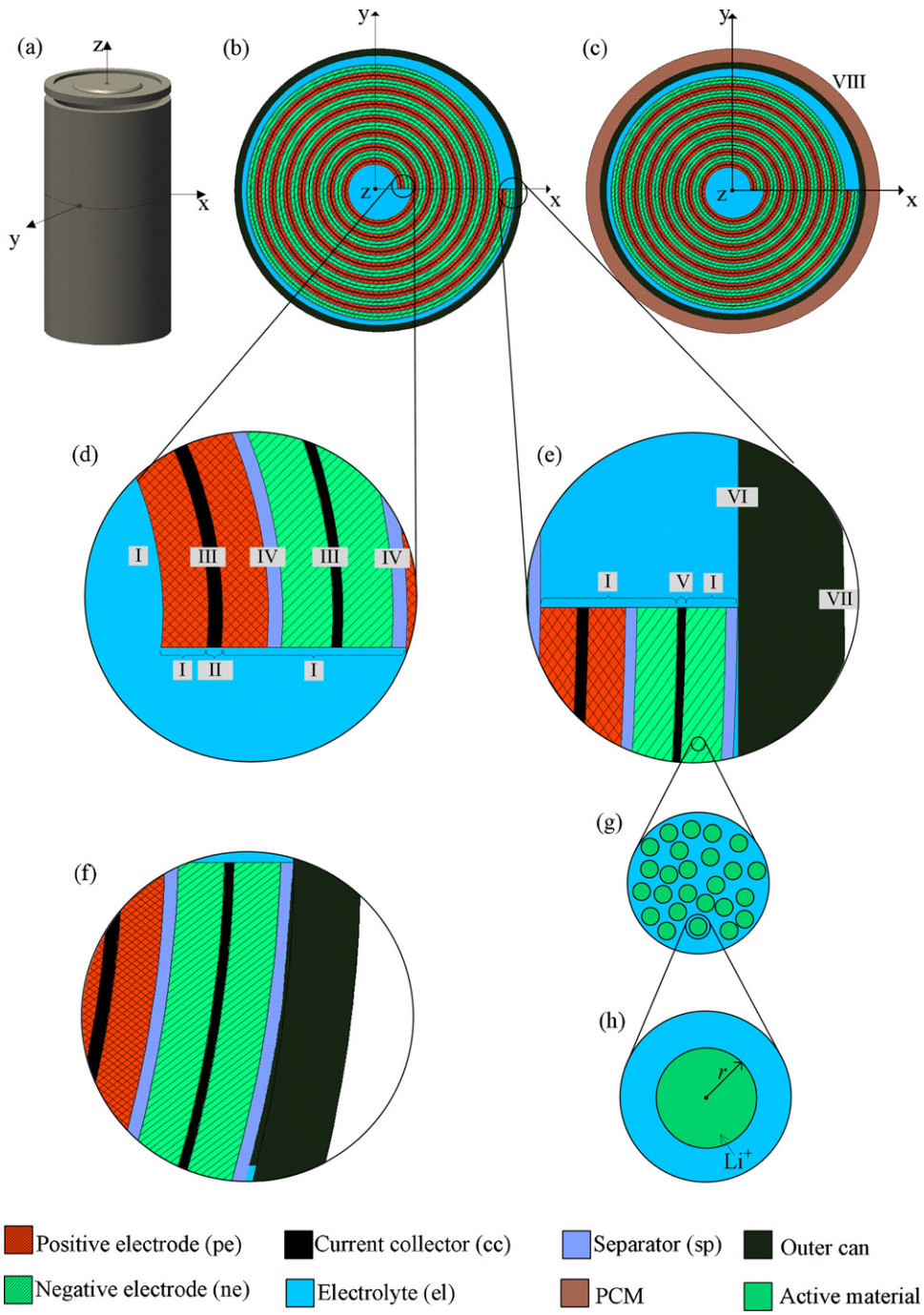

Fig. 1. Schematic of (a) a 18650 Li-ion battery, (b) cross-section of the 18650 battery showing the spiral-wound jelly roll, (c) cross section of the battery with PCM surrounding it, (d) various functional layers in the jelly roll with the roman numerals indicating the interfaces of these layers at the inner end of the spiral, (e) outer end of the spiral with the interfaces of various layers shown by the roman numerals, (f) modified computational domain, see *numerics*, (g) agglomerate structure in the negative electrode (*positive electrode also exhibits similar structure) and, (h) diffusion of lithium in active material in the electrodes on the microscale.

negative electrode (ne), current collector (cc) and separator (sp) – are wound up in the form of a jelly roll. We have taken the dimensions of the various functional layers from a Sony cell [27] with the number of wounds determined to be 15 based on the diameter of the battery and the thickness of the wounds.

Generally, the porous electrodes consist of active material, conductive filler additive, binder and liquid electrolyte (el). In this study, the active material in the negative electrode is $Li_{\mathfrak{x}}C_6$ and in the positive electrode it is $Li_{\mathfrak{y}}Mn_2O_4$. The salt is $LiPF_6$ in a nonaqueous 1:2 liquid mixture of ethylene carbonate and dimethyl carbonate. The electrochemical reactions that occur at the electrode/electrolyte interface during charge and discharge are then

$$Li_{\mathfrak{x}}C_6 \underset{\text{Charge}}{\overset{\text{Discharge}}{\rightleftarrows}} C_6 + \mathfrak{x}Li^+ + \mathfrak{x}e^-,$$

$$Li_{\mathfrak{y}-\mathfrak{x}}Mn_2O_4 + \mathfrak{x}Li^+ + \mathfrak{x}e^- \underset{\text{Charge}}{\overset{\text{Discharge}}{\rightleftarrows}} Li_{\mathfrak{y}}Mn_2O_4,$$

where $\mathfrak{x}$ is the stoichiometric coefficient or the number of moles of lithium present in the graphite structure, C_6, and $\mathfrak{y}$ is the number

Table 1
Parameters.

Parameter	Unit	cc (−)	ne	sp	pe	cc (+)	Reference
c_l^0	mol m^{-3}	–		2×10^3		–	[10]
c_p	J (kg K)$^{-1}$	3.8×10^2	7.0×10^2	7.0×10^2	7.0×10^2	8.7×10^2	[15]
c_s^0	mol m^{-3}	–	1.5×10^4	–	3.9×10^3	–	[10]
c_s^{max}	mol m^{-3}	–	2.6×10^4	–	2.3×10^4	–	[10]
D_l	m^2 s^{-1}	–	7.5×10^{-11}			–	[10]
D_s	m^2 s^{-1}	–	3.9×10^{-14}	–	1.0×10^{-13}	–	[10]
E_{a,D_l}	kJ mol^{-1}	–		10		–	[15]
E_{a,D_s}	kJ mol^{-1}	–	4	–	20	–	[15]
E_{a,σ_l}	kJ mol^{-1}	–		20		–	[15]
h	m			60×10^{-3}			–
$\mathfrak{h}$	W m^{-2} K^{-1}			5			–
i_{app} (1 C rate)	A m^{-2}			4.5×10^5			–
k	W (m K)$^{-1}$	3.8×10^2	0.05×10^2	0.01×10^2	0.05×10^2	2.0×10^2	[15]
R_b	m			9×10^{-3}			–
$\mathfrak{R}$	m	–	12.5×10^{-6}	–	8.5×10^{-6}	–	[10]
T_{amb}, T_{ref}	K			298.15			[15]
w_i	m	18×10^{-6}	88×10^{-6}	25×10^{-6}	80×10^{-6}	25×10^{-6}	[27]
α_a, α_c	–	–	0.5	–	0.5	–	[10]
ε_p	–	–	0.14	–	0.19	–	[10]
ε_l	–	–	0.36	0.72	0.44	–	[10]
ε_f	–	–	0.03	–	0.07	–	[10]
θ_i^0	–	–	0.56	–	0.17	–	[10]
ρ	kg m^{-3}	9.0×10^3	1.9×10^3	1.2×10^3	4.1×10^3	2.7×10^3	[10,15]
σ_s	S m^{-1}	6.0×10^7	1×10^2	–	3.8	3.8×10^7	[15]

of moles of lithium in the spinel structure of manganese dioxide Mn_2O_4; Li^+ is the lithium ion.

The materials for the positive and negative current collectors and the outer can are aluminum, copper and stainless steel, respectively.

The PCM, which is coated around the battery (Fig. 1c), is taken to be paraffin wax impregnated in a graphite matrix. Paraffin wax has a high latent heat but a low thermal conductivity, whence the graphite matrix is provided to enhance the heat transfer rate between the cell and the ambient by conduction [1,28]. Overall, PCMs have the advantage of storing and releasing heat within a narrow temperature range as latent heat. However, most of the PCMs have a low thermal conductivity [29] and various attempts have been carried out to improve the conductivity and in turn, the efficiency of the thermal energy storage [28]. In addition, factors like mechanical strength and electrical properties will constrain the thickness and type of the PCM that can be employed.

The length scales ranging from the agglomerate level on the order of 10^{-7} m to the cell level on the order of 10^{-1} m are resolved: the transport in the cell on length scales larger than that of the agglomerates (Fig. 1g) is referred to as the transport at the *macroscale*, which includes mass transfer in the electrolyte describing the movement of mobile ionic species, material balances, current flow and electroneutrality based on concentrated-solution theory [30], electronic charge conduction in the solid phase and energy transfer in the solid/liquid phases (Fig. 1b–f); the diffusion of ions in the active material in the electrodes is referred to as the transport at the *microscale*, which includes diffusion of lithium in the active material of the porous electrodes (Fig. 1g).

The main postulates and features of the model are as follows:

1. *Reduction in dimensionality*. The 3D battery (Fig. 1a) is reduced to a 2D cross-section (1b) through the middle of the battery, which is justified by the following arguments: first, insulated conditions for the energy flux are prescribed at the top and bottom surface of the battery (z-direction in Fig. 1a), which is a common assumption [19,31,32,18,22,25]. Second, as a first approximation, we assume that the air temperature is constant around the battery, whence the temperature difference, ΔT_z, inside the battery in the axial direction is zero; i.e., $\Delta T_z = 0$. Third, potential losses in the axial direction in the current collectors are negligible at leading order, since the potential drop in the z-direction, $\Delta\phi_{s,z} \sim i_{app}h/\sigma_s \approx 10^{-4}\,\text{V} \ll E_{cell} \sim 1\,\text{V}$, for typical operating and material properties: $i_{app} \sim 10^6\,\text{A m}^{-2}$ (~1 C-rate), $h \sim 10^{-3}$ m, $\sigma_s \sim 10^7\,\text{S m}^{-1}$, where i_{app} is the applied current density, h is the height of the battery, σ_s is the electrical conductivity and E_{cell} is the cell voltage. Fourth, the placement of current collecting tabs on the behavior of the cell is assumed to be negligible.

   For the resulting 2D cross-section, we prescribe the current as entering from the innermost boundary of the current collector (II) and leaving at the outermost current-collector boundary (V), which is justified by the potential drop in the tangential direction, $\Delta\phi_{s,t}$, around the total wound of length, $\mathcal{L}$, which is negligible at leading order compared to the overall cell voltage; i.e., $\Delta\phi_{s,t} \sim i_{app}\mathcal{L}/\sigma_s \approx 10^{-2}\,\text{V} \ll E_{cell} \sim 1\,\text{V}$, for a typical length of a wounded layer, $\mathcal{L} \sim 10^{-1}$ m. Note that this condition leads to errors when the C-rate is around 10 or higher, since $i_{app} \sim 10^7\,\text{A m}^{-2}$ (~10 C-rate), such that $\Delta\phi_{s,t} \sim i_{app}\mathcal{L}/\sigma_s \approx 10^{-1}\,\text{V} < E_{cell} \sim 1\,\text{V}$. Here, we limit the discussion to C-rates from one to five.
2. *Natural convection*. Natural convection in the type of PCM that we consider here has been shown to be negligible [33]. Inside the battery, we postulate negligible natural convection as a first approximation by letting gravity act in the z-direction, in which there are no temperature/concentration gradients due to the conditions outlined in #1 above; we note, however, that one could extend the model to include natural convection [34–37].
3. *Electrochemistry and related phenomena*. Side reactions inside the battery and double-layer capacitance are not considered, which is, again, a common assumption [14,38,39].

Table 2
PCM, electrolyte, and outer can properties.

Parameter	Unit	PCM [1]	Electrolyte [22]	Outer can
c_p	J (kg K)$^{-1}$	1980	2055	475
k	W (m K)$^{-1}$	16.6	0.6	44.5
ρ	kg m^{-3}	866	1129.95	7850
L	J kg^{-1}	181×10^3	–	–
T_s	K	325	–	–
T_l	K	328	–	–
ξ	–	0.9 (graphite alone)	–	0.8

Table 3
Constants in $U_{ref,i}$, $\partial U_{ref,i}/\partial T$, and σ_l expressions [10,15].

Constant	Unit	Value	Constant	Unit	Value	Constant	Unit	Value
$\mathfrak{n}_1$	mV K^{-1}	344.1347	$\mathfrak{p}_3$	mV K^{-1}	−26.0645	$\mathfrak{N}_3$	–	−3.0
$\mathfrak{n}_2$	–	−32.9633	$\mathfrak{p}_4$	mV K^{-1}	12.7660	$\mathfrak{N}_4$	V	10
$\mathfrak{n}_3$	–	8.3167	$\mathfrak{p}_5$	mV K^{-1}	4.3127	$\mathfrak{N}_5$	–	−2000
$\mathfrak{n}_4$	–	1	$\mathfrak{p}_6$	–	0.5715	$\mathfrak{P}_1$	V	4.1983
$\mathfrak{n}_5$	–	749.0756	$\mathfrak{p}_7$	mV K^{-1}	−0.1842	$\mathfrak{P}_2$	V	0.0565
$\mathfrak{n}_6$	–	−34.7909	$\mathfrak{p}_8$	–	−0.5169	$\mathfrak{P}_3$	–	−14.5546
$\mathfrak{n}_7$	–	8.8871	$\mathfrak{p}_9$	–	0.0462	$\mathfrak{P}_4$	–	8.6094
$\mathfrak{n}_8$	mV K^{-1}	−0.8520	$\mathfrak{p}_{10}$	mV K^{-1}	1.2816	$\mathfrak{P}_5$	V	−0.0275
$\mathfrak{n}_9$	mV K^{-1}	0.3622	$\mathfrak{p}_{11}$	–	−4.9916	$\mathfrak{P}_6$	–	0.9984
$\mathfrak{n}_{10}$	mV K^{-1}	0.2698	$\mathfrak{p}_{12}$	mV K^{-1}	−0.0904	$\mathfrak{P}_7$	–	0.4924
a_0	S m^{-1}	1.0793×10^{-2}	$\mathfrak{p}_{13}$	–	−20.9669	$\mathfrak{P}_8$	–	−1.9011
a_1	S m^2 mol^{-1}	6.7461×10^{-4}	$\mathfrak{p}_{14}$	–	−12.5788	$\mathfrak{P}_9$	V	−0.1571
a_2	S m^5 mol^{-2}	-5.2245×10^{-7}	$\mathfrak{p}_{15}$	mV K^{-1}	0.0313	$\mathfrak{P}_{10}$	–	−0.0474
a_3	S m^8 mol^{-3}	1.3605×10^{-10}	$\mathfrak{p}_{16}$	–	31.7663	$\mathfrak{P}_{11}$	V	0.8102
a_4	S m^{11} mol^{-4}	-1.1724×10^{-14}	$\mathfrak{p}_{17}$	–	−22.4295	$\mathfrak{P}_{12}$	–	−40
$\mathfrak{p}_1$	mV K^{-1}	−4.1453	$\mathfrak{N}_1$	V	−0.16	$\mathfrak{P}_{13}$	–	−0.1339
$\mathfrak{p}_2$	mV K^{-1}	8.1471	$\mathfrak{N}_2$	V	1.32		–	

4. *Material properties*. Uniform distribution of active materials of uniform size in the electrodes and PCM is assumed. Further, phase change for the PCM does not occur at a single temperature but rather over a given melting range, which is assumed to be captured reasonably well with a linear relation between latent heat in the 'mushy' region – where a liquid and solid phases coexist – of the PCM. The emissivity of PCM is taken to be the emissivity of pure graphite alone.
5. *Microscale properties*. The active material is assumed to be spherical; i.e., we only need to consider the radial direction at the microscale.
6. *Contact resistance*. The contact resistance between the PCM and the battery as well as between functional layers is assumed to be negligible as a first approximation.

The governing equations, boundary conditions and constitutive relations are summarized in Appendices A–D. The various parameters and constants are summarized in Tables 1–3.

3. Numerics

The commercial finite-element solver, COMSOL Multiphysics 4.1 [40], was employed to solve the 2D model after importing the geometry from AutoCAD 2011 [41], in which the 2D spiral-wound battery with/without PCM was created with the helix command by setting the height of the helix to zero (z-direction). The wounds were drawn one after the other starting from the center ($x = 0, y = 0$) in order to avoid interference of the various layers that occurred when all the wounds were drawn in a single step. The imported geometry appeared as a curve in COMSOL, whence it had to be coerced to a solid, followed by splitting the formed solid into separate subdomains representing the various functional layers. In addition, the narrowing gap of liquid electrolyte between the jelly roll and the outer can, as illustrated in Fig. 1f, was dealt with by treating the electrolyte present in the vicinity of the region where the jelly roll touches the outer can as part of the latter.

Linear elements were implemented for all dependent variables: ϕ_s, ϕ_l, c_l, c_s^{surf}, T and c_s^{avg}; the direct solver UMFPACK was chosen as linear solver with a relative convergence tolerance of 10^{-3}; and solutions for all models were tested for mesh independence.

Charge and discharge currents, i_{app}, were applied at the respective boundaries with a smoothed Heaviside function.

Furthermore, in order to avoid numerical instabilities due to negative values in the current density when the local state of charge (SOC) approaches unity (i.e., fully charged), a relational operator

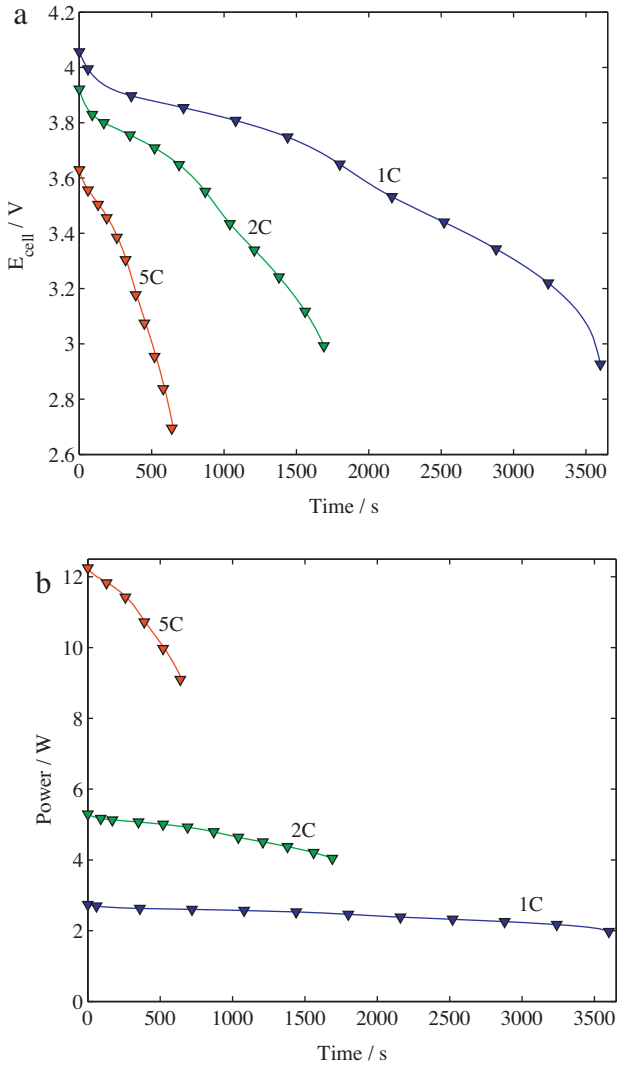

Fig. 2. (a) Cell voltage vs time and (b) power vs time for galvanostatic discharge at various C-rates with (symbols) and without PCM (lines).

was introduced for the exchange current density and local SOC, to ensure that the former does not become negative or exactly zero:

$$i_0 = Fk_0\sqrt{c_l c_s^{surf}\left[\left(c_s^{\max} - c_s^{surf}\right)\left(c_s^{\max} > c_s^{surf}\right) + c^*\right]}, \quad (1)$$

$$\theta_{pe} = \min\left(\frac{c_s^{surf}}{c_s^{\max}}, 1\right); \quad (2)$$

here, i_0 is the exchange current density, F is the Faraday's constant, k_0 is the reaction rate constant, c_l is the concentration of Li-ions in the electrolyte, c_s^{surf} is the concentration of Li-ions on the surface of the active material, $c_s^{\max}$ is the maximum concentration of Li-ions in the active material, θ_{pe} is the local SOC of the positive electrode, and $c^* = 10^{-12}$ mol m^{-3} is a negligible concentration chosen such that it does not affect the solution at leading order; i.e., $c^* \ll c_s^{\max} - c_s^{surf}$.

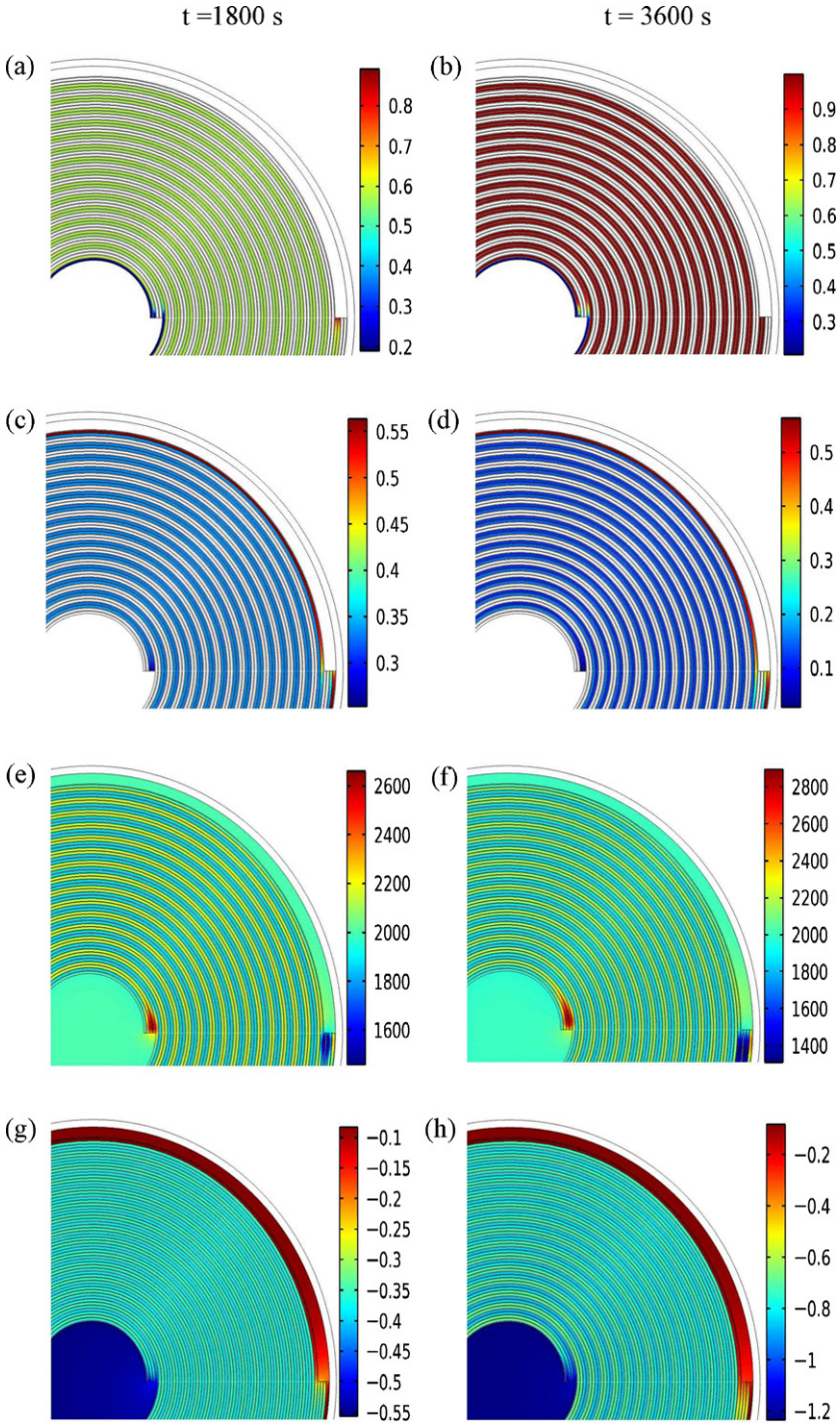

Fig. 3. Local distribution of the following dependent variables at t = 1800 s and t = 3600 s during discharge at 1 C-rate: SOC of positive electrode (a, b), SOC of negative electrode (c, d), lithium ion concentration in the electrolyte (e, f), and liquid phase potential (g, h).

The relational operators are introduced only for the positive electrode since the latter determines the capacity of the considered battery; more on this later in the discussion.

All computations were carried out on a workstation with two quad-core processors (3.2 GHz, with a total of eight processor cores) and a total of 64 GB random access memory (RAM).

4. Results and discussion

In the following, we will first study the behavior during discharge of a spiral-wound lithium-ion battery without a passive thermal-management system, such that only natural convection and radiation provide heat transfer with the surrounding. (We focus on the discharge process, since charging exhibits a similar behavior.) Thereafter, we compare the behavior of the cell with a PCM layer surrounding the battery.

4.1. Discharge and power curves

We start with the global behavior in terms of cell voltage and power during discharge for three different C-rates of the battery, as depicted in Fig. 2a and b. Overall, the battery discharge occurs, as expected, first gradually with decreasing cell voltage and power with respect to time, followed by a sharp drop towards the end of discharge. From the numerical point-of-view, the latter is reflected in a slowing convergence rate and requires the introduction of relational operators as introduced in *Numerics* earlier. Further, we note that the discharge curves are more or less the same for a battery with and without PCM; more on this later in the discussion.

4.2. Edge and geometry effects

In a spiral-wound Li-ion cell, the inner and outer ends of the spiral-wound jelly roll – see Fig. 1d and e respectively – are exposed to the liquid electrolyte both in the core as well as in the gap between the jelly roll and the outer can. Furthermore, the innermost layer comprising the positive electrode is only in contact with the electrolyte in the core and a current collector in the first wound; similar for the negative layer in the outermost wound, which is only in contact with a current collector and the separator layer. These edge and geometrical aspects from the spiral-wound geometry can thus be expected to give rise to localized effects and deviations from the average behavior. This is indeed the case, as can be inferred from Fig. 3, for the SOC, lithium-ion concentration in the electrolyte and liquid-phase potential during discharge at 1 C-rate halfway through, $t = 30$ min, and at the end, $t = 60$ min, for a lithium-ion battery without PCM. Here, two main features are apparent: first, is the uniformity in the interior of the cell and second, the expected deviations that occur at the inner and outer edges of the spiral wounds. For example, the SOC of the positive electrode at the inner edge of the spiral half-way through the discharge is around 0.2 (Fig. 3a), which is close to the initial SOC of 0.17; at the outer edge of the spiral and in the interior, the SOC is around 0.9 and 0.55 respectively. There is thus a lack of lithium-ions in the first wound, and an excess in the outer. At the end of the discharge, the SOC approaches 1 for the positive electrode except at the inner edge of the spiral where it is around 0.3 (Fig. 3b). The same phenomena are observed for the negative electrode (albeit reversed) as well as for the lithium-ion concentration and liquid-phase potential. These findings, in turn, suggest that the positive electrode at the inner edge of the spiral and the negative electrode at the outer edge of the spiral are not completely utilized – hence, these regions can be left uncoated while manufacturing a battery.

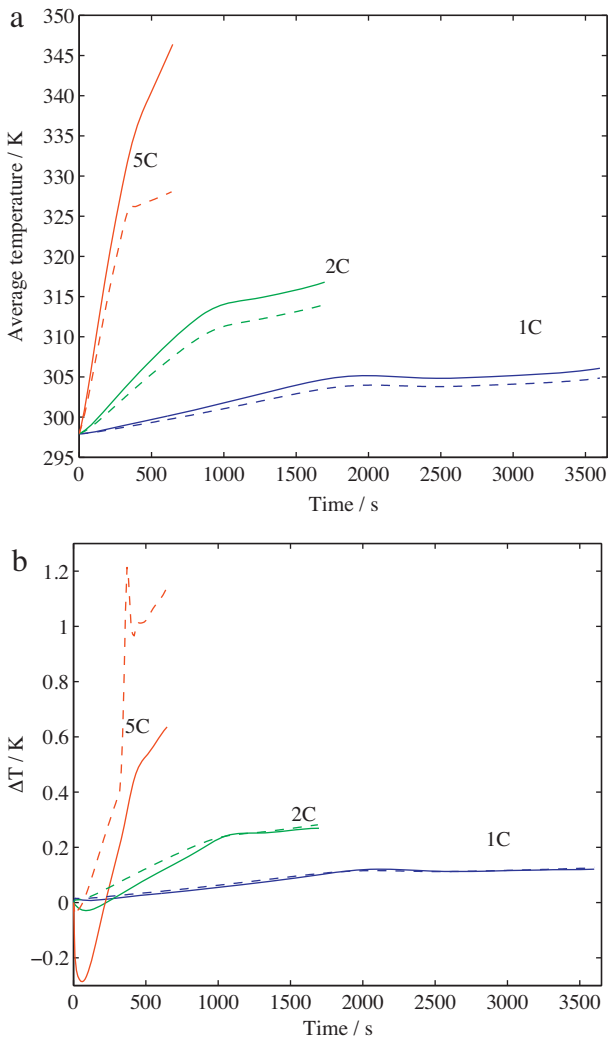

Fig. 4. Time history of (a) the average battery temperature and (b) the temperature difference between the battery core and the surface during discharge at various rates with (dotted) and without PCM (continuous).

4.3. Heat generation and thermal behavior

As alluded to in the introduction, thermal management is key in ensuring not only a safe operation but also to improve the cycle-life of a lithium-ion battery. In this case, the battery without a PCM is only cooled through natural convection and radiation, which gives rise to a significant temperature increase inside the cell during discharge, as shown in Fig. 4a. The temperature increases by around 8 K, 20 K, and 50 K above the ambient temperature for discharge rates of 1 C, 2 C, and 5 C, respectively, with a maximum temperature of 350 K reached at the end of discharge at the highest C-rate considered here, which indicates the need for a thermal management system. The radiation from the cell accounts for around 60% of the total heat transfer to the ambient as compared to 40% by natural convection. The temperature differential, ΔT, between the core and the outer can of the battery (Fig. 4b) is negligible compared to the overall, average temperature inside the battery; i.e. $\Delta T/T_{avg} \sim 10^{-3} \ll 1$, which indicates that the energy transport is mainly limited by the energy exchange with the ambient.

The rise in temperature originates from the electrochemical reaction and ohmic heating as charge is passed through the battery. The total heat generation rate and the contribution from each of the heat sources (see Eq. (D.6)) during discharge at 1 C-rate and 5 C-rate

are shown in Fig. 5a and b respectively. At a 1 C-rate, the reversible heat generation is higher than the other sources, amounting for nearly 50% of the total heat generation, followed by ohmic and irreversible heating. The reason can be traced back to the functional form of $\partial U_{ref,i}/\partial T$ given by Eqs. (D.7) and (D.8), which determines the behavior of the reversible heating with time: at a 1 C-rate, the reversible heat is negative initially and then it changes sign as the discharge proceeds, whereas the other heat sources are always positive. The ohmic heat generation starts rising during the initial period of discharge due to the currents that are passed through the battery and then almost becomes a constant for the rest of the discharge.

At a 5 C-rate, however, the ohmic heat generation is the highest contributor, amounting for nearly 50% of the total heat generation, followed by the irreversible and the reversible heat sources. The ohmic heat generation becomes increasingly larger due to the increasing current flow through the battery. However, a drop in the ohmic heat generation is observed after the initial increase unlike 1 C rate where it remains constant. The increase in battery temperature is mirrored by a decrease in the electric resistance, whence ohmic heating decreases during the discharge; in the herein derived model, the electric resistance of the battery is coupled with the temperature-dependent ionic conductivity and mass diffusivity in the solid phase. In contrast, the irreversible heating is almost constant with time with a slight increase towards the end of discharge.

A comparison of the total heat generation (Fig. 5a and b) with the power delivered by the battery (Fig. 2b) suggests that nearly 10% of the battery power is lost as heat at a 1 C-discharge rate; in comparison, 25% is lost through heat for the 5 C-rate.

Besides noting the relative magnitude of the various heat sources during discharge, it is also of interest to see which layer contributes the most to the heat generation (Fig. 5c and d): the negative electrode generates most of the heat, amounting to nearly 60% of the total heat both at 1 C and 5 C-rates, followed by the positive and then by the remaining layers. The reason for this behavior can be found in the ohmic and reversible heating, which are higher in the negative electrode than in the positive electrode due to lower ionic conductivity and the thicker, less porous nature of the negative electrode – the former is mainly dependent on the material properties and the latter are design-adjustable parameters. The heat generation in the current collector, electrolyte and separator, on the other hand, only comprise ohmic heating, whence they remain almost constant throughout the galvanostatic discharge.

Finally, we address the local temperature distribution, as illustrated in Fig. 6, half-way and at the end of discharge for a 1 C-rate. Compared to the other dependent variables discussed earlier, the temperature does not exhibit any edge effects;

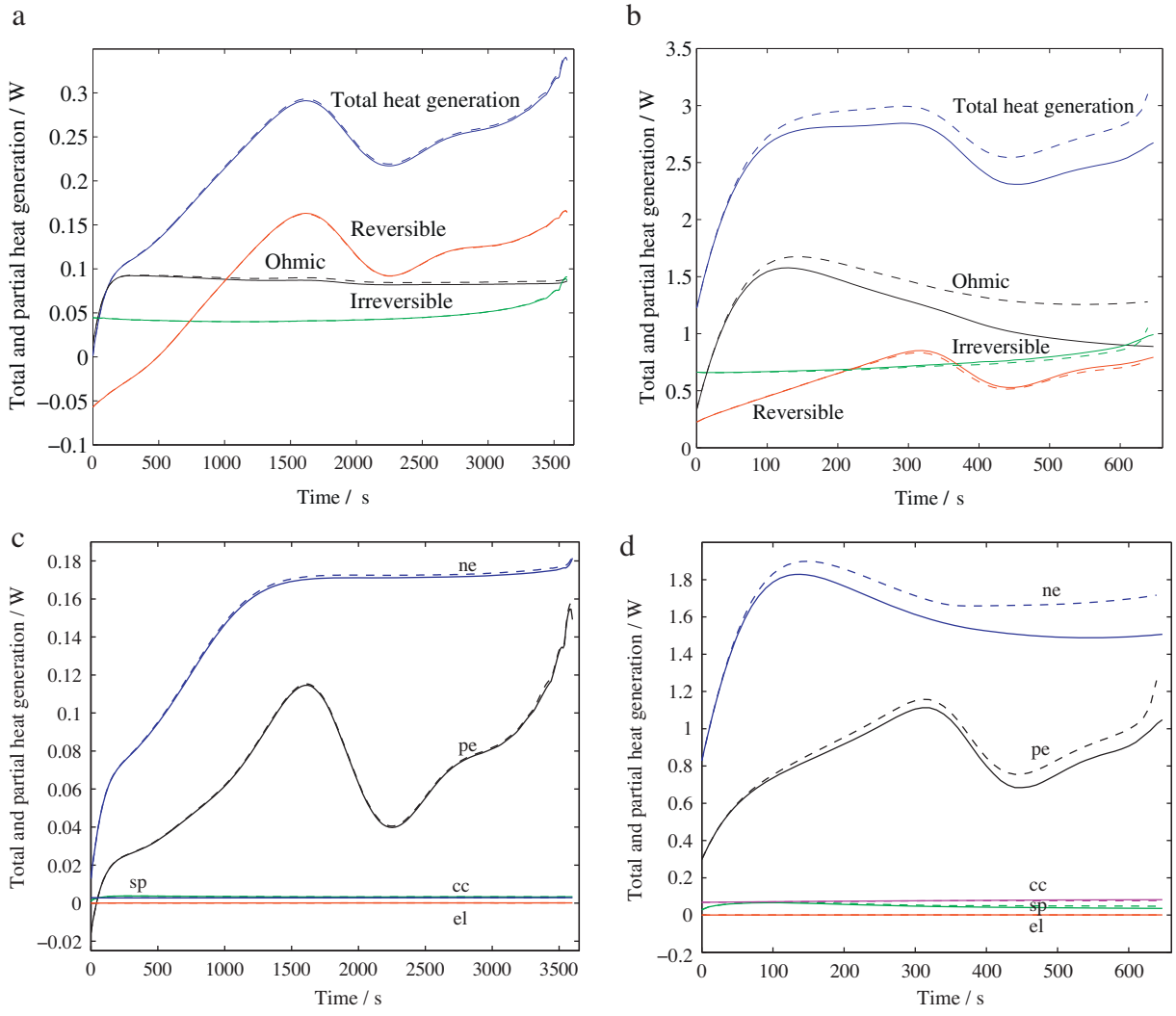

Fig. 5. Time history of heat generation by various sources (a, b), total heat generation and heat generation in various layers (c, d) during discharge at 1 C and 5 C-rates with (dotted) and without PCM (continuous).

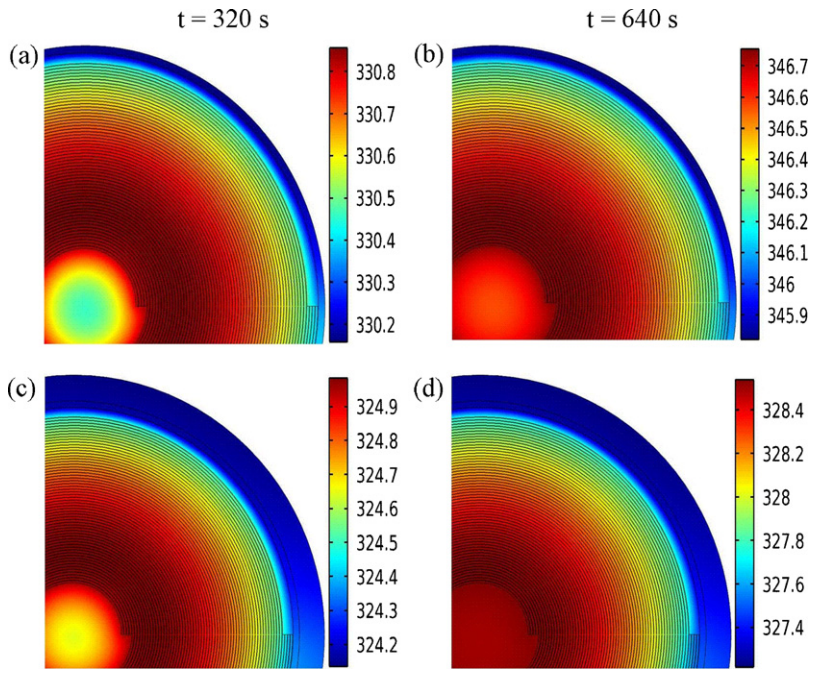

Fig. 6. Local distribution of temperature at $t = 320$ s and $t = 640$ s: without PCM (a, b), with PCM (c, d) during discharge at 5 C-rate.

instead, the temperature distribution is near-to axially symmetric (z-axis).

4.4. Passive thermal management

Thus far, we have seen that the limiting heat removal from the cell by natural convection and radiation is responsible for the overall temperature increase and that the temperature distribution inside the cell is axially symmetric with an overall temperature gradient that is negligible compared to the average temperature in the battery. One approach to manage the thermal envelope could be in the form of forced or mixed external convection with air/liquid through active thermal management; another approach, and the one we pursue here, is through passive thermal management with a PCM as an additional layer surrounding the battery cell. In essence, the disadvantage of doing so is that the additional layer effectively adds additional resistance to heat removal from the battery; the advantage, however, is that doing so increases the thermal capacitance.

Returning to Fig. 2, we note that the discharge curves and power characteristics remain unaffected at leading order when a PCM layer with thickness of 1 mm is added to the cell – which, at first sight, would suggest that the passive thermal management is ineffective and unnecessary. In contrast, however, the average temperature (Fig. 4a) is lowered as compared to the same cell without the PCM, whereas the average temperature gradient inside the cell (Fig. 4b) is slightly higher. The former can be explained by the increase in the thermal capacitance of the system (battery + PCM) and the latter by the increased resistance to energy transfer out of the system. Further, the PCM has not yet reached its melting temperature under the discharge rates of 1 C and 2 C, whence the advantage of cooling through phase-change is not realized in these two cases. Under a discharge rate of 5 C, however, the heat generated by the battery increases its temperature to the melting range of the PCM, such that the battery is around 18 K cooler at the end of discharge as compared to without PCM – a substantial decrease. Furthermore, at a 5 C-rate, the temperature differential with PCM reaches a maximum of 1.2 K and then decreases rapidly owing to the drop in heat generation from the battery and the loss of heat to the ambient through convection and radiation; it increases again as heat generation starts to rise.

The layer with PCM also affects the heat generated by the battery at the 5 C-rate whereas at a 1 C-rate, there is no noticeable difference in heat generation, as shown in Fig. 5. Overall, the total heat generation increases by nearly 7% with PCM as compared to without at a 5 C-rate. This corresponds to the fact that the presence of PCM keeps the battery temperature lower as compared to the battery without PCM, which in turn lowers the ionic conductivity and mass diffusivity, thus increasing the resistance of the battery and finally leading to an increase in ohmic heating.

The PCM also maintains the temperature uniformity within the cell unlike forced-convection cooling [1,2], for which appreciable temperature differences between the core and the outer surface of the battery can be established. The temperature distribution inside the battery with the PCM is shown in Fig. 6c and d, in which the temperature rise from $t = 320$ s to $t = 640$ s is 16 K without PCM and 4 K with PCM at a 5 C-rate. The maximum temperature difference between the core of the battery and the outer can is 0.8 K without PCM and 1 K with PCM and this increase in gradient is due to the additional resistance for heat transfer to the ambient as mentioned above.

The state of the PCM can readily be identified as solid, liquid or mushy based on the temperature of the system. When it is in the mushy region, another parameter is needed to exactly define its state: the liquid fraction. For 1 C and 2 C-rates, since the PCM has not yet reached its melting temperature range, the liquid fraction is zero whereas at a 5 C rate, the wax present inside the graphite matrix starts melting, but does not reach a completely liquid state at the end of discharge as the liquid fraction is 0.7 (Fig. 7), indicating that it lies in the two phase or the mushy region. The volume of the PCM in the layer surrounding the battery should thus be chosen so that it is not completely liquid at the end of discharge to ensure cooling throughout the discharge. The drop at around 360 s in the liquid fraction during discharge mirrors the drop in the heat generation inside the battery, as shown earlier in Fig. 5b.

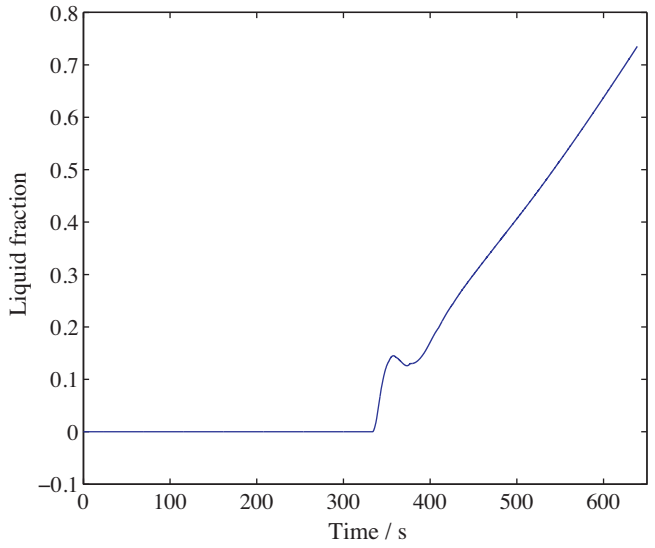

Fig. 7. Liquid fraction of PCM vs time during discharge at 5 C-rate.

With this model, one can, e.g., optimize the thickness of the PCM while accounting for the operating conditions of the battery.

5. Conclusions

A two-dimensional coupled thermal–electrochemical model for a commercially available spiral-wound Li-ion battery has been presented and analyzed for discharge in terms of geometry and edge effects as well as in terms of passive thermal management with a PCM. The reduction in dimensionality was justified through scaling arguments and negligible heat flux in the axial direction of the battery.

In summary, the active material is depleted to a larger extent at the outer end of the spiral for the positive electrode and at the inner end of the spiral for the negative electrode than at the remaining parts, where it is utilized uniformly. Further, reversible heat generation is the highest contributor at lower discharge rates around 1 C-rate, whereas ohmic heating is the highest contributor among the heat generation sources for higher discharge rates. The findings suggest that the battery design can be optimized in order to, for example, reduce the ohmic heating by improving the electrolyte conductivity and the design-adjustable parameters like the thickness and porosity of the electrodes.

A passive thermal management system has been evaluated by wrapping a PCM around the battery, which reduces the average temperature of the battery for higher discharge rates: here, around 5 C-rate.

The model can be extended to include the effect of current collecting tabs, other active materials, and the axial dimension if the heat flux is not negligible by extruding the geometry. Furthermore, thermal runaway can be simulated by including the additional reaction heats and temperature dependence of the reaction rates. Finally, the numerical procedure to implement the geometry and mathematical formulation could be automated [42] to allow for wide-ranging parameter studies as well as multi-objective optimization of a Li-ion battery cell with passive thermal management.

Acknowledgements

The financial support of the National University of Singapore and SERC MODERN Project Grant R-263-000-507-305 is gratefully acknowledged.

Appendix A.

A.1. Governing equations (macroscale)

The mathematical model comprises conservation of species and charge in the solution- and the solid-phase as well as the conservation of energy [2,10,15,43]:

$$\nabla \cdot \mathbf{i}_s = -J\,(\text{pe, ne, cc}), \tag{A.1}$$

$$\nabla \cdot \mathbf{i}_l = J\,(\text{pe, ne, sp, el}), \tag{A.2}$$

$$\varepsilon_l \frac{\partial c_l}{\partial t} + \nabla \cdot \mathbf{N}_l = \frac{J}{F}\,(\text{pe, ne, sp, el}), \tag{A.3}$$

$$\rho C_p \frac{\partial T}{\partial t} + \nabla \cdot \mathbf{q} = Q(\text{pe, ne, sp, cc, el}), \tag{A.4}$$

$$\rho \frac{\partial H}{\partial t} + \nabla \cdot \mathbf{q} = 0(\text{PCM}), \tag{A.5}$$

where the fluxes are given by

$$\mathbf{i}_s = -\sigma_s^{eff} \nabla \phi_s, \tag{A.6}$$

$$\mathbf{i}_l = -\sigma_l^{eff} \nabla \phi_l + \frac{2RT\sigma_l^{eff}}{F}\left(1 - t_+^0\right) \nabla(\ln c_l), \tag{A.7}$$

$$\mathbf{N}_l = -D_l^{eff} \nabla c_l + \frac{t_+^0 \mathbf{i}_l}{F}, \tag{A.8}$$

$$\mathbf{q} = -k \nabla T. \tag{A.9}$$

In the above equations, $\mathbf{i}_s$ is the solid-phase current density, J is the transfer current per unit volume, σ_s^{eff} is the effective conductivity of the solid phase, ϕ_s is the solid phase potential, $\mathbf{i}_l$ is the solution phase current density, σ_l^{eff} is the effective electric conductivity of the solution phase, ϕ_l is the solution phase potential, R is the universal gas constant; T is the absolute temperature, F is the Faraday's constant, t_+^0 is the transference number of the cation, ε_l is the volume fraction of electrolyte in the electrodes and the separator, and $\mathbf{N}_l$ is the molar flux of the cations; ρ is the effective density of the various functional layers, C_p is the effective specific heat capacity, $\mathbf{q}$ is the conductive heat flux, H is the enthalpy of the PCM, Q is the heat generation per unit volume, D_l^{eff} is the effective diffusion coefficient in the liquid/solution phase, and k is the effective thermal conductivity; the electrolyte is a binary electrolyte with the concentration of the electrolyte c_l defined as [30] $c_l = c_+/\nu_+ = c_-/\nu_-$, where c_+ and c_- are the concentrations of the cations and anions respectively, and ν_+ and ν_- represent the number of cations and anions produced by the dissociation of one mole of electrolyte. (The governing equations are applicable in the layers mentioned inside parentheses.)

Appendix B.

B.1. Governing equations (microscale)

At the microscale, lithium diffuses into the spherical active material particles (Fig. 1g), whence the conservation of lithium inside the active material can be stated as

$$\frac{\partial c_s}{\partial t} = \frac{1}{r^2}\frac{\partial}{\partial r}\left(r^2 D_s \frac{\partial c_s}{\partial r}\right), \tag{B.1}$$

where $c_s(x, y, r, t)$ is the concentration of protons in the active material particle of the electrode; t represents the time, D_s is the diffusion coefficient of lithium in the active material, and r is the radial coordinate inside an agglomerate. Here we employ the diffusion length

approach [44] and a polynomial approximation [45], such that the governing equations in the microscale are reduced to

$$\frac{D_s}{l_s}(c_s^{surf} - c_s^{avg}) = -\frac{i_f}{F}, \tag{B.2}$$

$$\frac{dc_s^{avg}}{dt} = -\frac{3i_f}{F\mathfrak{R}}; \tag{B.3}$$

c_s^{surf} and c_s^{avg} are the volume-averaged surface and average concentrations of Li-ion in the active material, i_f is the charge transfer current density and $\mathfrak{R}$ is the radius of the active material in the electrodes.

Appendix C.

C.1. Boundary and initial conditions

At the interface I between the electrode/electrolyte or the separator/electrolyte (see Fig. 1d and e for placement of roman numerals), we specify continuity for the energy flux as well as the ionic flux of lithium ions (ionic current), whereas insulation is specified for the solid-phase current:

$$\mathbf{n}\cdot\mathbf{i}_s = 0, \qquad \mathbf{n}\cdot\mathbf{i}_l|_{\mathrm{I}_+} = \mathbf{n}\cdot\mathbf{i}_l|_{\mathrm{I}_-}, \qquad \mathbf{n}\cdot\mathbf{N}_l|_{\mathrm{I}_+} = \mathbf{n}\cdot\mathbf{N}_l|_{\mathrm{I}_-}\ (\mathrm{I}), \tag{C.1}$$

The current density is prescribed at the positive current collector in the inner end of the spiral:

$$\mathbf{n}\cdot\mathbf{i}_s = -i_{app}\,(\mathrm{II}). \tag{C.2}$$

At the current collector/electrode interfaces, continuity of energy flux and solid-phase current is specified; insulation is specified for the ionic flux and current:

$$\mathbf{n}\cdot\mathbf{i}_s|_{\mathrm{III}_+} = \mathbf{n}\cdot\mathbf{i}_s|_{\mathrm{III}_-}, \qquad \mathbf{n}\cdot\mathbf{q}|_{\mathrm{III}_+} = \mathbf{n}\cdot\mathbf{q}|_{\mathrm{III}_-},$$

$$\mathbf{n}\cdot\mathbf{i}_l = \mathbf{n}\cdot\mathbf{N}_l = 0\,(\mathrm{III}). \tag{C.3}$$

At the electrode/separator interfaces, we define continuity of energy flux and ionic flux as well as ionic current and since there is no flow of electrons across the interface, insulation for solid phase current is defined.

$$\mathbf{n}\cdot\mathbf{i}_s = 0, \qquad \mathbf{n}\cdot\mathbf{i}_l|_{\mathrm{IV}_+} = \mathbf{n}\cdot\mathbf{i}_l|_{\mathrm{IV}_-},$$

$$\mathbf{n}\cdot\mathbf{q}|_{\mathrm{IV}_+} = \mathbf{n}\cdot\mathbf{q}|_{\mathrm{IV}_-}\mathbf{n}\cdot\mathbf{N}_l|_{\mathrm{IV}_+} = \mathbf{n}\cdot\mathbf{N}_l|_{\mathrm{IV}_-}\ (\mathrm{IV}). \tag{C.4}$$

The negative current collector at the outer end of the spiral is grounded:

$$\phi_s = 0\,(\mathrm{V}). \tag{C.5}$$

At the electrolyte/can interface, there is continuity of energy flux and no flow of ions:

$$\mathbf{n}\cdot\mathbf{q}|_{\mathrm{VI}_+} = \mathbf{n}\cdot\mathbf{q}|_{\mathrm{VI}_-}, \qquad \mathbf{n}\cdot\mathbf{i}_l = \mathbf{n}\cdot\mathbf{N}_l = 0(\mathrm{VI}). \tag{C.6}$$

At the outer surface of the can, both convection and radiation is considered:

$$\mathbf{n}\cdot\mathbf{q} = \mathfrak{h}(T - T_a) + \xi\beta(T^4 - T_a^4)(\mathrm{VII}). \tag{C.7}$$

When the battery is covered with PCM, there is continuity of energy flux from the can to the PCM and on the outer surface of the PCM (VIII), Newton's law of cooling is specified along with radiative energy transfer as given by Eq. (C.7). In Eqs. (C.1)–(C.7), $\mathbf{n}$ denotes the unit normal vector for a given boundary or interface, i_{app} is the applied current density, ξ is the emissivity, and β is the Stefan–Boltzmann constant. The battery is discharged under galvanostatic conditions at various current densities.

At $t = 0$, we prescribe

$$c_s = c_s^{avg} = c_s^0, \qquad c_l = c_l^0 \tag{C.8}$$

$$\phi_s = \begin{cases} 0 & (\mathrm{ne}) \\ \phi_s^0 & (\mathrm{pe}) \end{cases} \tag{C.9}$$

$$\phi_l = \phi_l^0\,(\mathrm{ne, pe, sp}) \tag{C.10}$$

$$T = T_0 \tag{C.11}$$

Appendix D.

D.1. Constitutive relations and parameters

The source term, J, is expressed as

$$J = \begin{cases} \mathcal{A}i_f & (\mathrm{ne, pe}) \\ 0 & (\mathrm{sp, cc, el}) \end{cases}, \tag{D.1}$$

where $\mathcal{A}$ is the specific surface area for the faradaic reaction per unit volume; the local charge transfer current density is given by the Butler–Volmer equation for electrode kinetics

$$i_f = i_0\left\{\exp\left(\frac{\alpha_a\eta F}{RT}\right) - \exp\left(-\frac{\alpha_c\eta F}{RT}\right)\right\}. \tag{D.2}$$

Here, i_0 is the exchange current density, α_a and α_c are the anodic and cathodic transfer coefficients and η is the overpotential. The specific interfacial area is related to the particle radius, volume void fraction of filler ϵ_f, polymer matrix ϵ_p, and, solution phase [10] as

$$\mathcal{A} = \frac{3(1-\epsilon_l-\epsilon_f-\epsilon_p)}{\mathfrak{R}}. \tag{D.3}$$

The exchange current density is given by

$$i_0 = Fk_0\sqrt{c_l(c_s^{\max} - c_s^{surf})c_s^{surf}}; \tag{D.4}$$

k_0 is the reaction rate constant and $c_s^{\max}$ is the maximum lithium concentration in the electrodes. The overpotential is defined as

$$\eta = \phi_s - \phi_l - U_{ref,i}^{eff}, \quad i = \mathrm{ne, pe} \tag{D.5}$$

in which U_{ref}^{eff} is the effective open circuit potential of the electrode with respect to the solid lithium electrode. The internal heat generation rate Q [15] is defined as

$$Q = J\eta + JT\frac{\partial U_{ref,i}}{\partial T} + \sigma_s^{eff}(\nabla\phi_s)^2 + \sigma_l^{eff}(\nabla\phi_l)^2 + \frac{2RT\sigma_l^{eff}}{F}(1-t_+^0)\nabla(\ln c_l)\cdot\nabla\phi_l, \quad i = \mathrm{ne, pe} \tag{D.6}$$

The entropic change as a function of state of charge for the negative electrode is expressed as

$$\frac{\partial U_{ref,\mathrm{ne}}}{\partial T} = \frac{\mathfrak{n}_1\exp(\mathfrak{n}_2\theta_{\mathrm{ne}} + \mathfrak{n}_3)}{\mathfrak{n}_4 + \mathfrak{n}_5\exp(\mathfrak{n}_6\theta_{\mathrm{ne}} + \mathfrak{n}_7)} + \mathfrak{n}_8\theta_{\mathrm{ne}} + \mathfrak{n}_9\theta_{\mathrm{ne}}^2 + \mathfrak{n}_{10}, \tag{D.7}$$

and for the positive electrode as

$$\frac{\partial U_{ref,\mathrm{pe}}}{\partial T} = \mathfrak{p}_1 + \mathfrak{p}_2\theta_{\mathrm{pe}} + \mathfrak{p}_3\theta_{\mathrm{pe}}^2 + \mathfrak{p}_4\theta_{\mathrm{pe}}^3 + \mathfrak{p}_5\exp(\mathfrak{p}_6\theta_{\mathrm{pe}}) + \mathfrak{p}_7\exp\left(-\frac{\theta_{\mathrm{pe}} + \mathfrak{p}_8}{\mathfrak{p}_9}\right)^2 + \mathfrak{p}_{10}\sin(\mathfrak{p}_{11}\theta_{\mathrm{pe}}) + \mathfrak{p}_{12}\sin(\mathfrak{p}_{13}\theta_{\mathrm{pe}} + \mathfrak{p}_{14}) + \mathfrak{p}_{15}\sin(\mathfrak{p}_{16}\theta_{\mathrm{pe}} + \mathfrak{p}_{17}), \tag{D.8}$$

in which $i\mathfrak{n}$ and $i\mathfrak{p}$ [15] are constants obtained from curve fitting with experimental data; θ_{ne} and θ_{pe} denote the state of charge of the negative and positive electrodes respectively, and are defined as

$$\theta_{\mathrm{ne}} = \theta_{\mathrm{pe}} = \frac{c_s^{surf}}{c_s^{\max}}. \tag{D.9}$$

The first term on the right-hand-side (RHS) in the heat generation, Eq. (D.6), captures the irreversible heat generation arising due to the reaction that is responsible for the deviation of the potential from the equilibrium potential; the second term is the reversible heat due to the changes in entropy; the third term quantifies the ohmic heating in the solid phase; and the last two terms reflect the ohmic heating in the solution phase. The overall state of charge of the battery here refers to the local state of charge of the positive electrode as the battery capacity is limited due to the positive electrode. The electrode capacity is defined as

$$C_i = w_i(1-\epsilon_l-\epsilon_f-\epsilon_p)\rho_i C_{th}, \quad i = \text{ne, pe}, \tag{D.10}$$

where w_i represents the thickness of the electrodes and C_{th} is the theoretical capacity of the electrode material (372 mAh g^{-1} for the negative electrode, and 148 mAh g^{-1} for the positive electrode). The total battery capacity will be the minimum of the two electrode capacities and in our case, the positive electrode has the minimum capacity.

The open-circuit potential of the two electrodes are taken from Doyle et al. [10]: for the positive electrode, we write

$$U_{ref,\text{pe}} = \mathfrak{P}_1 + \mathfrak{P}_2\ \tanh(\mathfrak{P}_3\theta_{\text{pe}} + \mathfrak{P}_4) + \mathfrak{P}_5\left(\frac{1}{(\mathfrak{P}_6-\theta_{\text{pe}})^{\mathfrak{P}_7}} + \mathfrak{P}_8\right) + \mathfrak{P}_9\ \exp\left(\mathfrak{P}_{10}\theta_{\text{pe}}^8\right) + \mathfrak{P}_{11}\ \exp(\mathfrak{P}_{12}(\theta_{\text{pe}} + \mathfrak{P}_{13})), \tag{D.11}$$

and for the negative electrode

$$U_{ref,\text{ne}} = \mathfrak{N}_1 + \mathfrak{N}_2\ \exp(\mathfrak{N}_3\theta_{\text{ne}}) + \mathfrak{N}_4\ \exp(\mathfrak{N}_5\theta_{\text{ne}}), \tag{D.12}$$

where $i\mathfrak{N}$ and $i\mathfrak{P}$ are constants obtained by curve fitting with experimental data.

The effective (i.e., temperature-dependent) open-circuit potential of an electrode is approximated by a first order Taylor-series expansion around a reference temperature T_{ref} [38]:

$$U_{ref,i}^{eff} = U_{ref,i} + \left(T - T_{ref}\right)\frac{\partial U_{ref,i}}{\partial T}, \ i = \text{ne, pe} \tag{D.13}$$

The effective conductivities and diffusivity are defined as

$$\sigma_s^{eff} = \sigma_s\varepsilon, \tag{D.14}$$

$$\sigma_l^{eff} = \sigma_l\varepsilon^{\gamma}, \tag{D.15}$$

$$D_l^{eff} = D_l\varepsilon^{\gamma}, \tag{D.16}$$

where γ is the Bruggemann constant.

The electrolyte conductivity is expressed as a function of concentration c_l [10]:

$$\sigma_l = \sum_{i=0}^{4} a_i c_l^i, \tag{D.17}$$

where a_i are constants.

The physical properties – diffusion coefficients (both solid and liquid) and electrical conductivity (liquid) – are dependent on temperature, the function of which is typically written in the form of an Arrhenius expression [15,38]:

$$\Theta(T) = \Theta(T_{ref})\ \exp\left[\frac{E_{a,\Theta}}{R}\left(\frac{1}{T_{ref}} - \frac{1}{T}\right)\right] \tag{D.18}$$

where $\Theta(T)$ is a placeholder for a temperature-dependent property, T_{ref} is a reference temperature, and $E_{a,\Theta}$ is the activation energy.

The diffusion length, l_s, for the spherical electrode particles is estimated as [44]

$$l_s = \frac{\mathfrak{R}}{5}. \tag{D.19}$$

The initial values of the solid phase and the liquid phase potential are given by

$$\phi_s^0 = U_{ref,\text{pe}}(\theta_{\text{pe}}^0) - U_{ref,\text{ne}}(\theta_{\text{ne}}^0), \tag{D.20}$$

$$\phi_l^0 = -U_{ref,\text{ne}}(\theta_{\text{ne}}^0), \tag{D.21}$$

where θ_{pe}^0 and θ_{ne}^0 denote the initial states of charge (SOC) of the positive and negative electrodes respectively. The solid-phase potential difference between the positive current collector at the inner end of the spiral and the negative current collector at the outer end of the spiral is defined as the cell voltage, E_{cell}:

$$E_{cell} = \phi_s|_{\text{II}} - \phi_s|_{\text{V}}. \tag{D.22}$$

The current density at which the battery becomes completely discharged in 1 h is taken as the 1 C-rate. (Complete discharge here implies the local SOC in the positive electrode reaches one.)

The phase change for the material considered here takes place over a given melting range, which is captured the following functional form, $H(T)$ [43]:

$$H(T) = \begin{cases} C_pT & \text{for } T < T_s \text{ (solid region)}, \\ C_pT + \dfrac{T-T_s}{T_l-T_s}L & \text{for } T_s \le T \le T_l \text{(mushy region)}, \\ C_pT + L & \text{for } T > T_l \text{ (liquid region)}, \end{cases} \tag{D.23}$$

where L is the latent heat of the phase change and T_s and T_l are the start and end temperatures of the phase change respectively.

The average temperature for the battery is defined as

$$\left\langle T\right\rangle = \frac{1}{\pi R_b^2}\int\int_{\Omega} T(x,y)\,dA, \tag{D.24}$$

where R_b is the radius of the battery and Ω is the region of integration representing the entire battery as shown in Fig. 1b. The temperature differential is defined as

$$\Delta T = T|_{\mathfrak{r}=0} - \frac{1}{2\pi R_b}\oint_0^{2\pi R_b} T\,ds, \tag{D.25}$$

where $\mathfrak{r}$ is the radial coordinate and the second term on the right hand side represents the average temperature at the outer surface of the can. The total heat generation and the heat generation in various layers is defined as

$$\left\langle Q\right\rangle = h\int\int_{\Omega} Q\,dA \tag{D.26}$$

$$\left\langle Q_i\right\rangle = h\int\int_{\Omega} Q_i\,dA, \quad i = \text{ne, pe, sp, el, cc} \tag{D.27}$$

where h is the height of the battery considering only the jelly roll without the top cap assembly.

References

[1] R. Sabbah, R. Kizilel, J. Selman, S. Al-Hallaj, J. Power Sources 182 (2008) 630–638.
[2] S.A. Hallaj, J. Selman, J. Electrochem. Soc. 147 (9) (2000) 3231–3236.
[3] S.A. Khateeb, M.M. Farid, J.R. Selman, S. Al-Hallaj, J. Power Sources 128 (2004) 292–307.
[4] A. Mills, S. Al-Hallaj, J. Power Sources 141 (2005) 307–315.
[5] R. Kizilel, R. Sabbah, J.R. Selman, S. Al-Hallaj, J. Power Sources 194 (2009) 1105–1112.
[6] M.Y. Ramandi, I. Dincer, G.F. Naterer, Heat Mass Transfer 47 (2011) 777–788.
[7] T.M. Bandhauer, S. Garimella, T.F. Fuller, J. Electrochem. Soc. 158 (3) (2011) R1–R25.
[8] D. Bernardi, E. Pawlikowski, J. Newman, J. Electrochem. Soc. 132 (1) (1985) 5–12.
[9] M. Doyle, T.F. Fuller, J. Newman, J. Electrochem. Soc. 140 (6) (1993) 1526–1533.
[10] M. Doyle, J. Newman, J. Electrochem. Soc. 143 (6) (1996) 1890–1903.
[11] G.G. Botte, B.A. Johnson, R.E. White, J. Electrochem. Soc. 146 (3) (1999) 914–923.
[12] M.W. Verbrugge, B.J. Koch, J. Electrochem. Soc. 146 (3) (1999) 833–839.
[13] L. Song, J.W. Evans, J. Electrochem. Soc. 147 (6) (2000) 2086–2095.
[14] W. Gu, C. Wang, J. Electrochem. Soc. 147 (8) (2000) 2910–2922.

[15] V. Srinivasan, C.Y. Wang, J. Electrochem. Soc. 150 (1) (2003) A98–A106.
[16] V.R. Subramanian, V. Boovaragavan, V. Ramadesigan, M. Arabandi, J. Electrochem. Soc. 156 (4) (2009) A260–A271.
[17] K. Onda, T. Ohshima, M. Nakayama, K. Fukuda, T. Araki, J. Power Sources 158 (2006) 535–542.
[18] Y.I. Cho, H. Frank, G. Halpert, J. Power Sources 21 (1987) 183–194.
[19] T. Evans, R. White, J. Electrochem. Soc. 136 (8) (1989) 2145–2152.
[20] J.N. Harb, R.M. LaFollette, J. Electrochem. Soc. 146 (3) (1999) 809–818.
[21] T. Hatchard, D. MacNeil, A. Basu, J. Dahn, J. Electrochem. Soc. 148 (7) (2001) A755–A761.
[22] S.-C. Chen, Y.-Y. Wang, C.-C. Wan, J. Electrochem. Soc. 153 (4) (2006) A637–A648.
[23] G.-H. Kim, A. Pesaran, R. Spotnitz, J. Power Sources 170 (2007) 476–489.
[24] D.H. Jeon, S.M. Baek, Energy Convers. Manage. 52 (2011) 2973–2981.
[25] X. Zhang, Electrochim. Acta 56 (2011) 1246–1255.
[26] K. Smith, C.-Y. Wang, J. Power Sources 160 (2006) 662–673.
[27] B.A. Johnson, R.E. White, J. Power Sources 70 (1998) 48–54.
[28] A. Mills, M. Farid, J. Selman, S. Al-Hallaj, Appl. Thermal Eng. 26 (2006) 1652–1661.
[29] B. Zalba, J.M. Marin, L.F. Cabeza, H. Mehling, Appl. Thermal Eng. 23 (2003) 251–283.
[30] J. Newman, K.E. Alyea (Eds.), Electrochemical Systems, 3rd edition, Wiley-Interscience, 2004.
[31] E. Kalu, R. White, J. Electrochem. Soc. 140 (1) (1993) 23–31.
[32] P.M. Gomadam, R.E. White, J.W. Weidner, J. Electrochem. Soc. 150 (10) (2003) A1339–A1345.
[33] X. Py, R. Olives, S. Mauran, Int. J. Heat Mass Transfer 44 (2001) 2727–2737.
[34] R. Pollard, J. Newman, J. Electrochem. Soc. 128 (3) (1979) 491–502.
[35] F.H. Bark, F. Alavyoon, Appl. Sci. Res. 53 (1-2) (1994) 11–34.
[36] F.H. Bark, F. Alavyoon, J. Fluid Mech. 290 (1995) 1–28.
[37] K.I. Borg, K.E. Birgersson, F.H. Bark, J. Appl. Electrochem. 37 (11) (2007) 1287–1302.
[38] W.B. Gu, C.Y. Wang, in: S. Surampudi, R.A. Marsh, Z. Ogumi, J. Prakash (Eds.), The Electrochemical Society Proceedings Series, Pennington, NJ, 2000.
[39] P.M. Gomadam, J.W. Weidner, R.A. Dougal, R.E. White, J. Power Sources 110 (2002) 267–284.
[40] Comsol Multiphysics 3.5a, http://www.comsol.com.
[41] AutoCAD, STUDENT VERSION, 2011, http://students.autodesk.com/.
[42] H. Ly, E. Birgersson, M. Vynnycky, A. Sasmito, J. Electrochem. Soc. 156 (10) (2009) B1156–B1168.
[43] M.N. Ozisik (Ed.), Heat Conduction, 2nd edition, Wiley-Interscience, 1993.
[44] C.Y. Wang, W.B. Gu, B.Y. Liaw, J. Electrochem. Soc. 145 (10) (1998) 3407–3417.
[45] V.R. Subramanian, J.A. Ritter, R.E. White, J. Electrochem. Soc. 148 (11) (2001) A444–A449.